Chemical Engineering Journal 522 (2025) 167730

Contents lists available at ScienceDirect

Chemical Engineering Journal

journal homepage: www.elsevier.com/locate/cej

# Synergistic defect engineering in β-$MnO_2$ nanorods for energy-efficient photocatalytic air purification

Jiejing Kong [a,b,*], Hongzhao Chen [a,b], Zhida Li [a,b], Miaoqiu Tang [a,b], Yi Wang [a,b], Yunlong Guo [a,b], Weiping Zhang [a,b], Taicheng An [a,b]

[a] Guangdong Key Laboratory of Environmental Catalysis and Health Risk Control, Guangdong-Hong Kong-Macao Joint Laboratory for Contaminants Exposure and Health, Institute Environmental Health and Pollution Control, Guangdong University of Technology, Guangzhou 510006, China
[b] Guangdong Engineering Technology Research Center for Photocatalytic Technology Integration and Equipment, Guangdong Basic Research Center of Excellence for Ecological Security and Green Development, School of Environmental Science and Engineering, Guangdong University of Technology, Guangzhou 510006, China

ARTICLE INFO

*Keywords:*
β-$MnO_2$ nanorods
Oxygen vacancies
Visible-light-driven photocatalysis
Toluene mineralization
Mixed valence

ABSTRACT

A scalable strategy combining surfactant-assisted hydrothermal synthesis with controlled acidification was developed to fabricate β-$MnO_2$ nanorods with engineered oxygen vacancies and mixed $Mn^{3+}/Mn^{4+}$ valence states. Structural characterization revealed that the nanorods exhibit a 16-fold higher specific surface area (52.62 $m^2 \cdot g^{-1}$) than commercial β-$MnO_2$ (3.26 $m^2 \cdot g^{-1}$), along with compressive lattice strain and abundant defect sites. These attributes synergistically enhanced visible-light absorption, charge separation, and oxygen activation, enabling exceptional photocatalytic toluene mineralization under ambient conditions. The catalyst achieved 95 % toluene degradation and 93 % mineralization within 40 min, a 7.2-fold increase in mineralization efficiency over the commercial one. In situ DRIFTS analysis identified key intermediates (benzyl alcohol, benzaldehyde, benzoic acid) and confirmed complete oxidation to $CO_2$, validating defect-mediated deep mineralization. Photothermal synergy at 90 °C further accelerated kinetics, yielding a 5.6-fold rate increase for high-concentration toluene (750 ppm). The nanorods retained >90 % efficiency over five cycles and sustained high activity in continuous-flow operation (>10 h) under visible light irradiation, demonstrating industrial viability for energy-efficient VOC remediation. This work provides a cost-effective strategy for designing transition metal oxide catalysts with tunable electronic and morphological properties for air purification.

## 1. Introduction

The degradation of indoor air quality has emerged as a pressing global health concern, exacerbated by prolonged human exposure to enclosed environments in modern urbanized societies [1,2]. Among indoor pollutants, volatile organic compounds (VOCs), particularly toluene, are pervasive due to their widespread use in construction materials and their documented association with chronic health risks, including respiratory disorders and neurotoxic effects [3,4]. Conventional remediation approaches, such as physical adsorption and thermal catalytic oxidation, remain constrained by intrinsic limitations, including finite regeneration capacity, high energy demands, and operational complexity [5]. While noble metal catalysts (e.g., Pt, Au) exhibit exceptional activity in VOC degradation, their prohibitive costs, susceptibility to sintering, and limited stability under practical conditions hinder large-scale implementation [6–8]. Transition metal oxides, in contrast, offer a viable alternative due to their cost-effectiveness, thermal robustness, and adaptable electronic structures, positioning them as promising candidates for sustainable air purification [9–11]. Within this category, manganese oxides ($MnO_2$) have attracted significant interest owing to their polymorphic versatility, redox-active nature, and oxygen mobility [12,13]. However, their practical utility in photocatalytic applications is often compromised by inefficient charge carrier dynamics and sluggish surface reaction kinetics.

Recent advancements in defect engineering and nanostructuring have aimed to address the inherent limitations of $MnO_2$-based catalysts. Oxygen vacancies ($O_{vac.}$) play dual roles by trapping photogenerated electrons to suppress charge recombination and activating molecular oxygen into reactive intermediates such as superoxide radicals ($\bullet O_2^-$) [14]. Concurrently, mixed $Mn^{3+}/Mn^{4+}$ oxidation states enhance redox

* Corresponding author at: Guangdong Key Laboratory of Environmental Catalysis and Health Risk Control, Guangdong-Hong Kong-Macao Joint Laboratory for Contaminants Exposure and Health, Institute Environmental Health and Pollution Control, Guangdong University of Technology, Guangzhou 510006, China.
*E-mail address:* kongjj3@gdut.edu.cn (J. Kong).

https://doi.org/10.1016/j.cej.2025.167730
Received 14 July 2025; Received in revised form 11 August 2025; Accepted 24 August 2025
Available online 25 August 2025

cycling efficiency, a key factor for sustained catalytic activity [15,16]. Despite these improvements, existing $MnO_2$ systems often exhibit condition-dependent performance. For example, ultrathin $MnO_2$ nanosheets achieve 80 % formaldehyde removal at 105 °C but rely on elevated temperatures, limiting their practicality in ambient environments [17]. Similarly, $MnO_2$ nanoflowers efficiently degrade dyes under acidic conditions but underperform in neutral or gaseous-phase systems [18]. These examples highlight a critical gap: most $MnO_2$ catalysts operate optimally only under specific thermal, chemical, or phase conditions, restricting their versatility for real-world air purification. Commercial $MnO_2$ further suffers from agglomerated morphologies and low surface areas, which hinder mass transfer and accelerate deactivation via pore blockage [19]. To overcome these challenges, one-dimensional $MnO_2$ nanorods have emerged as promising candidates due to their directional charge transport and exposed active facets [20]. However, the interplay between defect engineering, nanoscale morphology, and photocatalytic efficiency remains underexplored, particularly for recalcitrant pollutants like toluene under ambient conditions. Integrating these elements could unlock synergistic effects, enabling robust VOCs degradation at mild operating parameters.

In this study, we address these challenges through the rational design of defect-engineered β-$MnO_2$ nanorods. By combining surfactant-assisted hydrothermal synthesis with controlled acidification, we construct $O_{vac.}$ and stabilize mixed $Mn^{3+}/Mn^{4+}$ valence states. This dual-functional strategy leverages the nanorod morphology to facilitate rapid toluene diffusion while utilizing lattice strain and defect clusters to optimize charge separation and oxygen activation pathways. The resultant catalyst demonstrates exceptional visible-light-driven photocatalytic activity, achieving near-complete toluene degradation and mineralization at ambient temperature. This work not only elucidates the interplay between structural and electronic properties in $MnO_2$-based systems but also provides a scalable framework for developing energy-efficient air purification technologies.

## 2. Experimental section

### 2.1. Preparation of β-$MnO_2$

All chemicals were of analytical grade and used without further purification. Scalable defect-engineered β-$MnO_2$ nanorods were synthesized via a surfactant-assisted hydrothermal method combined with controlled acidification. Specifically, $MnSO_4{\cdot}4H_2O$ was first finely ground in a mortar. Subsequently, 5.0 mL polyethylene glycol 400 (PEG-400) was added to homogenize the mixture. Finely ground $KMnO_4$ was then incorporated (molar ratio $MnSO_4{\cdot}4H_2O$: $KMnO_4$ = 2:3), followed by continuous blending for 0.5 h. The resulting slurry was transferred to a 100 mL Teflon-lined autoclave and hydrothermally treated at 90 °C for 24 h. After cooling, the product was centrifuged, washed with deionized water, and dried overnight at 105 °C. To engineer $O_{vac.}$, the dried sample was acidified in 2.0 mol/L $H_2SO_4$ for 2.0 h, followed by repeated centrifugation and washing until neutrality. The final defect-rich β-$MnO_2$ nanorods were obtained after drying at 105 °C for 10 h. Commercial β-$MnO_2$ (denoted as Com.β-$MnO_2$) was used for comparison.

### 2.2. Characterizations

The morphology, structure, surface elemental composition, and BET surface areas of the samples were characterized using scanning electron microscopy (SEM, TESCAN MIRA LMS, 30 keV), X-ray diffraction (XRD, Bruker D8 ADVANCE), X-ray photoelectron spectroscopy (XPS, Thermo Fisher Escalab 250Xi), and a specific surface area and pore size analyzer (Autosorb-iQ, USA). Optical properties were measured via UV–vis diffuse reflectance spectroscopy (DRS, Shimadzu UV-3600Plus) and photoluminescence spectroscopy (PL, HORIBA Fluorolog-3, using a 380 nm excitation wavelength xenon lamp). Photocurrent response was evaluated using an electrochemical workstation (Shanghai Chenhua Instrument Co., Ltd). Temperature-programmed reduction and desorption analyses ($H_2$-TPR, $O_2$-TPD, toluene-TPD) were performed on a chemisorption analyzer (TP-5078 Autochem, China). Electron paramagnetic resonance (EPR) spectra were acquired on a Bruker EMXPlus-10/12 spectrometer. $O_{vac.}$ measurements were conducted at 77 K (X-band, 9.84 GHz) with 4.00 G modulation amplitude and 100 kHz modulation frequency, under dark conditions and after 20 min of irradiation (300 W Xe lamp, λ: 400–780 nm). Photoinduced radicals were trapped using 5,5-dimethyl-1-pyrroline-N-oxide (DMPO). DMPO-•$O_2^-$ adducts (in methanol) and DMPO-•OH adducts (in $H_2O$) were measured at ambient temperature using 0.25 mg catalyst and 0.5 μL of 50 mM DMPO in 5 mL solvent, with spectra recorded after 3 min irradiation. The EPR signals are inherently mass-normalized due to the consistent catalyst mass (0.25 mg) used in all tests. In situ diffuse reflectance infrared Fourier transform spectroscopy (DRIFTS) of toluene adsorption/oxidation was performed on a Nicolet iS10 FTIR spectrometer equipped with a Harrick DRIFTS cell and liquid nitrogen-cooled MCT detector. Spectra (1000–3500 $cm^{-1}$, 4 cm-1 resolution, 16 scans) were collected under irradiation from a 300 W Xe lamp (λ: 400–780 nm) delivered via optical fiber. To quantitatively correlate DRIFTS observations with mineralization efficiency, exhaust gas from the DRIFTS cell was collected after 30 min of illumination under identical reaction conditions (1000 ppm toluene, diluted catalyst in KBr [1:100 mass ratio]). The gas was transferred to a Tedlar bag and analyzed for $CO_2$ concentration via GC (GC7900, Sci-Tech).

### 2.3. Visible light photocatalytic activity measurement

Photocatalytic reactions were conducted in a quartz reactor (CEL-GPRT100, Beijing China Education Au-light Co., Ltd.) using a 300 W Xe lamp strictly filtered with liquid optical and visible-light reflective filters to exclusively deliver irradiation within 400–780 nm (simulating AM1.5G solar spectrum, eliminating IR contributions). Temperature was maintained within ±1 °C via thermocouple monitoring and active water circulation to isolate photochemical effects. A 0.2 g catalyst sample was dispersed in a quartz vessel at the reactor base. For batch reactions, toluene (100, 350, or 750 ppm in dry air) was introduced. After achieving adsorption-desorption equilibrium during a 30-min dark period, irradiation commenced. Gas samples were periodically withdrawn for GC analysis (GC7900, Sci-Tech) to quantify toluene and $CO_2$ concentrations. For continuous reactions, a 100 ppm toluene/dry air stream was continuously fed. Following 30 min of stabilization in the dark, the lamp was activated. Toluene and $CO_2$ concentrations at the reactor outlet were automatically analyzed by GC (GC7900, Sci-Tech) every 10 min.

## 3. Results and discussion

### 3.1. Structural characterization

The XRD profiles (Fig. 1a) confirm the tetragonal rutile structure (β-phase, JCPDS-24-0735) for both synthesized and commercial β-$MnO_2$. Significantly, the synthesized β-$MnO_2$ exhibits a higher (110)/(002) intensity ratio (~21.7) than that of Com.β-MnO2 (~16.7), signifying preferential growth along the [001] crystallographic direction [21]. SEM characterization (Fig. S1a) corroborates this structural anisotropy, revealing uniformly dispersed nanorods (length: ~400 nm, diameter: 10–20 nm) with high morphological regularity. To further validate morphology and crystallinity, TEM and HRTEM analyses were performed. TEM (Fig. 1b) confirmed the nanorod structure. HRTEM (Fig. 1c) revealed distinct lattice fringes with an interplanar spacing of 0.311 nm, corresponding to the (110) plane of β-$MnO_2$. This orientation aligns with [001]-directed growth, consistent with XRD-derived preferential orientation. Notably, localized surface regions exhibit pits lacking lattice fringes (highlighted by yellow circles) and roughened edges, suggesting oxygen vacancy clusters and lattice distortions,

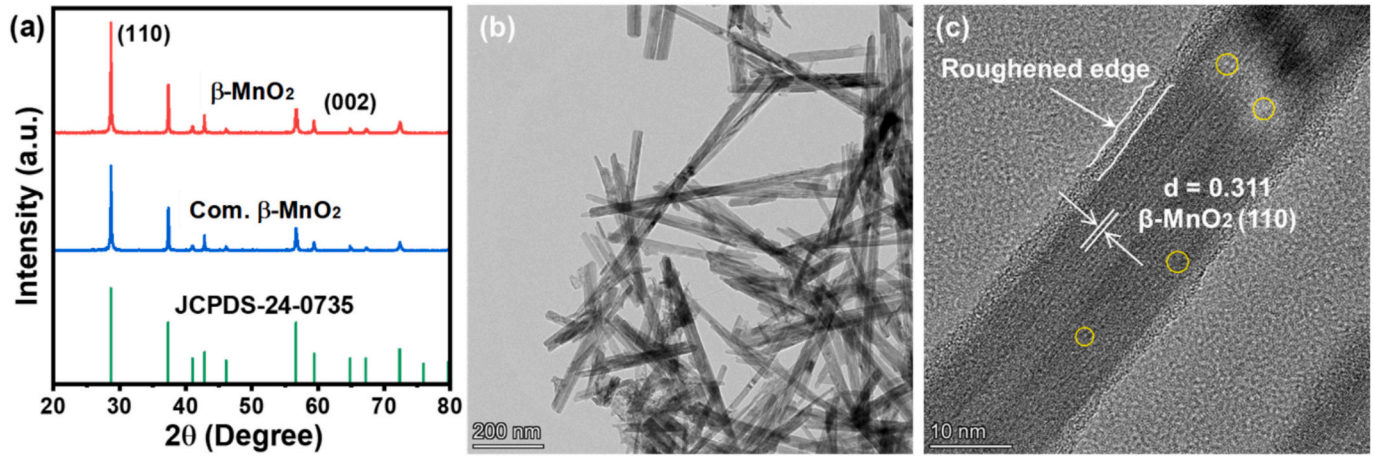


**Fig. 1.** (a) XRD patterns of the samples; (b) TEM and (c) HRTEM images of β-$MnO_2$.

supporting the defect engineering strategy. This contrasts sharply with Com.β-$MnO_2$, which consists of densely packed, amorphous microspheres with irregular surfaces that limit active site accessibility (Fig. S1b). BET analysis (Table S1) demonstrates a 16-fold higher specific surface area for the nanorods (52.62 $m^2 \cdot g^{-1}$) compared to Com.β-$MnO_2$ (3.26 $m^2 \cdot g^{-1}$), enabling efficient mass transfer. Complementary $N_2$ physisorption isotherms (Fig. S2) reveal $H_3$-type hysteresis loops in both samples, characteristic of slit-shaped mesopores [22]. Notably, Com.β-$MnO_2$ displays pronounced separation between adsorption/desorption branches, attributed to restricted pore connectivity within its agglomerated microstructure.

The Raman spectra unveil distinctive lattice modulation characteristics in β-$MnO_2$ nanorods (Fig. 2a). Compared to Com.β-$MnO_2$ nanoparticles (632.0 $cm^{-1}$), the nanorods exhibit a 7 $cm^{-1}$ blue shift in their dominant vibrational peak at 639.0 $cm^{-1}$. This phenomenon may originate from compressive lattice stress induced by one-dimensional confinement effects, analogous to a mechanically compressed spring, which shortens Mn—O bond lengths and enhances bond energy, thereby amplifying the $B_2g$ vibrational mode intensity [23]. Such stress fields likely facilitate localized charge redistribution, forming oriented $Mn^{4+}$–$O^-$ dipoles that optimize the surface migration pathways of photogenerated holes. Significantly, a distinctive Raman peak at 519.6 $cm^{-1}$, absent in Com.β-$MnO_2$, emerges exclusively in the defect-engineered β-$MnO_2$ nanorods. This signal, red-shifted by 18 $cm^{-1}$ from the theoretical $A_1g$ mode (538 $cm^{-1}$), arises from synergistic interactions between $Mn^{3+}$/$Mn^{4+}$ mixed valence states and $O_{vac.}$ clusters [24,25].

These spectral inferences gain quantitative validation through XPS

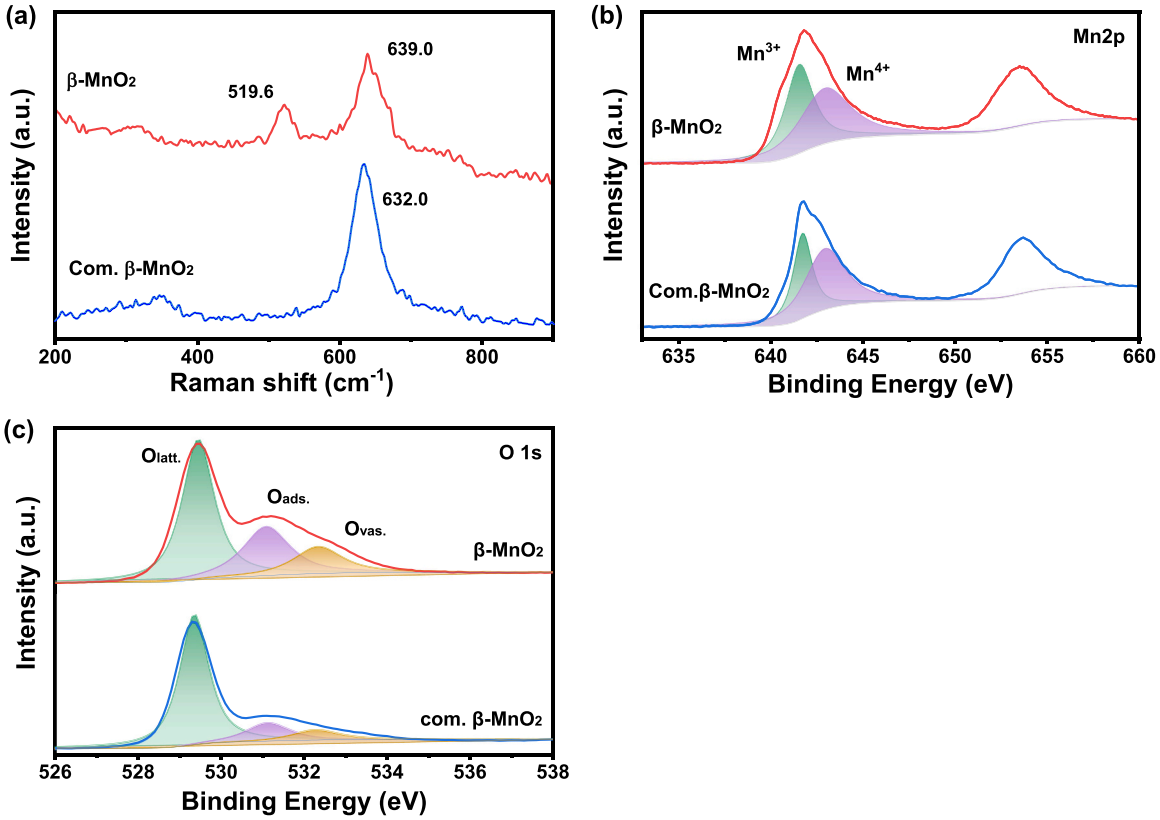


**Fig. 2.** (a) Raman spectra; (b) Mn 2p and (c) O1s XPS spectra of the samples.

deconvolution. Mn 2p analysis (Fig. 2b) resolves characteristic doublets at 641.7 eV (Mn $2p_{3/2}$) and 653.7 eV (Mn $2p_{1/2}$), confirming contributions from both $Mn^{3+}$ and $Mn^{4+}$ species [26,27]. Quantitative analysis (Table S2) confirms elevated $Mn^{3+}$ concentration in β-$MnO_2$ nanorods (47.2 %) compared to Com.β-$MnO_2$ (39.5 %). This enhanced $Mn^{3+}$ is often sociated with $O_{vac.}$ formation, as such defects often accompany mixed-valent manganese systems. Furthermore, the $Mn^{3+}$ enrichment likely induces Jahn-Teller distortions, generating localized lattice strain, that synergize with the Raman-observed lattice stress. Such coordinated structural perturbations may reconfigure surface electronic environments, and affect the oxygen configurations in β-$MnO_2$. O1s spectra (Fig. 2c) suggested the possible coexistence of three oxygen configurations in β-$MnO_2$: lattice oxygen ($O_{latt.}$, 529.4–529.5 eV), adsorbed oxygen species ($O_{ads.}$, 531.1 eV), and oxygen vacancies ($O_{vac.}$, 532.3 eV) [28]. Quantitative comparison (Table S3) indicated an apparent enhancement in reactive oxygen species for the synthesized β-$MnO_2$, with $O_{ads.}$ content increasing from 15.9 % to 28.4 % (78.6 % relative enhancement) and $O_{vac.}$ concentration rising from 9.6 % to 16.0 % (66.7 % increase) compared to Com.β-$MnO_2$.

### 3.2. Optical properties

The optical properties of the β-$MnO_2$ nanorods including light absorption, charge recombination dynamics, and radical generation, were systematically investigated and compared with Com.β-$MnO_2$. UV–Vis diffuse reflectance spectra (Fig. 3a) revealed broad absorption bands (400–1000 nm) for both β-$MnO_2$ nanorods and Com.β-$MnO_2$, attributed to d–d transitions of Mn ions and $Mn^{3+}$-induced mid-gap states from

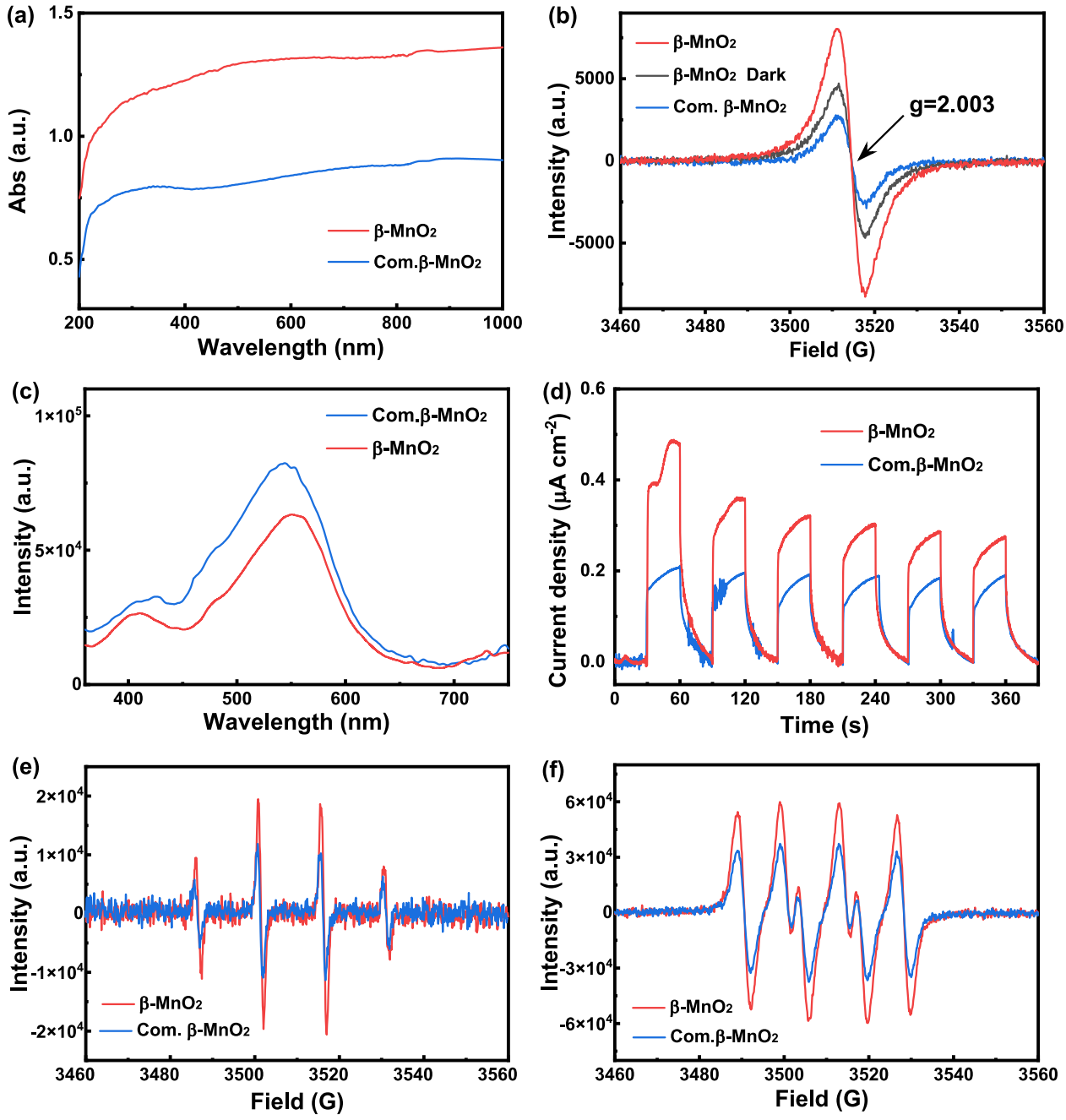


**Fig. 3.** (a) UV–vis diffuse reflectance spectra and (b) EPR spectra of the catalysts; (c) Photoluminescence spectra with an excitation of a Xe lamp and (d) time-dependent photocurrents of the samples under on-off visible light (λ = 400–800 nm) exposure pulse of 60 s with a constant bias of 0.2 V vs. Ag/AgCl electrode; (e) DMPO–•OH and (f) DMPO–$•O_2^-$ EPR spectra of the samples with a fixed catalyst loading (0.25 mg).

coexisting $Mn^{3+}/Mn^{4+}$ [29]. Notably, the β-$MnO_2$ nanorods exhibited enhanced absorption, stemming from synergistic electron transitions, lattice distortions, and band-structure modulation driven by elevated $Mn^{3+}$ content (Fig. 2b) [30,31].

EPR spectroscopy directly probes the light-responsive behavior of $O_{vac.}$ critical to this enhanced absorption. Under visible light, the synthesized β-$MnO_2$ nanorods exhibit a 3.1-fold stronger EPR signal at g = 2.003 than Com.β-$MnO_2$ and a 1.7-fold increase compared to their dark-state signal (Fig. 3b). This signal is primarily assigned to paramagnetic $V_O^{\bullet}$ species (single-electron trapped $O_{vac.}$) [32]. The significant light-induced signal amplification is characteristic of efficient photoinduced electron trapping at vacancy sites, corroborating the 66.7 % increase in $O_{vac.}$ concentration quantified by XPS (Fig. 2c). While minor contributions from carbonaceous radicals cannot be entirely ruled out, the collective evidence strongly supports vacancy-mediated electron trapping as the dominant mechanism. The inherently higher EPR intensity of the nanorods confirms their greater intrinsic $O_{vac.}$ concentration, quantitatively consistent with XPS data. Crucially, this efficient electron capture at $O_{vac.}$ sites could significantly suppresses charge recombination.

Photoluminescence (PL) and photocurrent measurements further validated the enhanced charge separation efficiency. The β-$MnO_2$ nanorods exhibited a 25 % reduction in PL intensity (Fig. 3c), indicating suppressed radiative recombination. Concurrently, transient photocurrent density (Fig. 3d) was 1.6 times higher (0.32 μA/$cm^2$) than that of Com.β-$MnO_2$ (0.20 μA/$cm^2$). These results demonstrate efficient charge separation within the mixed-valent system, where $Mn^{3+}$ acts as electron donors to reduce adsorbed $O_2$ (forming $\bullet O_2^-$) while simultaneously trapping photogenerated holes through oxidation to $Mn^{4+}$ [33]. This dual functionality synergistically suppresses charge recombination. The synergistic effects of $O_{vac.}$ and mixed valence also amplified the generation of reactive oxygen species. EPR spectra using DMPO spin-trapping confirmed significantly stronger signals for both DMPO-•OH and DMPO-$\bullet O_2^-$ under visible-light irradiation over the β-$MnO_2$ nanorods compared to Com.β-$MnO_2$ (Fig. 3e,f). This directly links the enhanced radical yields to the defect-rich surfaces of the engineered catalyst.

### 3.3. Defect-enhanced redox properties and pollutant adsorption

$H_2$-TPR and $O_2$-TPD analyses were employed to elucidate the enhanced reducibility and oxygen activation dynamics conferred by defects in the β-$MnO_2$ nanorods. Under dark conditions, $H_2$-TPR profiles (Fig. 4a) revealed two reduction peaks for β-$MnO_2$ nanorods at 363.7 °C ($MnO_2 \rightarrow Mn_3O_4$) and 461.3 °C ($Mn_3O_4 \rightarrow MnO$) [34,35]. Visible-light irradiation shifted these peaks downward by 8–11 °C to 352.5 °C and 443.4 °C, indicating enhanced reducibility due to photoinduced $Mn^{4+}/Mn^{3+}$ cycling and $O_{vac.}$-mediated lattice oxygen destabilization. Critically, the reduction temperatures for β-$MnO_2$ nanorods were ~ 63 °C lower than those of Com.β-$MnO_2$ (415.8 °C / 547.2 °C), confirming superior reducibility. This phenomenon stems from $O_{vac.}$-mediated destabilization of lattice oxygen and accelerated $Mn^{3+}/Mn^{4+}$ redox cycling, consistent with XPS quantification of Mn valence states and EPR detection of paramagnetic centers. While XPS and EPR are surface-sensitive, their alignment with bulk-sensitive $H_2$-TPR data suggests defect effects extend beyond surface regions.

Complementing these findings, $O_2$-TPD studies (Fig. 4b) identified four oxygen species desorbing across 100–800 °C: (i) physically adsorbed $O_2$ (< 200 °C), (ii) active surface oxygen ($O_{ads.}$, 200–300 °C), (iii) adsorbed atomic oxygen ($O^-$, 300–600 °C), and (iv) subsurface/bulk lattice oxygen ($O_{latt.}$, > 600 °C) [36,37]. In darkness, β-$MnO_2$ nanorods displayed a broad desorption peak centered at 355.3 °C (250–600 °C), assigned to $O_{ads.}$ and $O^-$ [36–39]. Visible-light irradiation shifted this peak to 310.3 °C, a 45 °C decrease, confirming photoactivation of

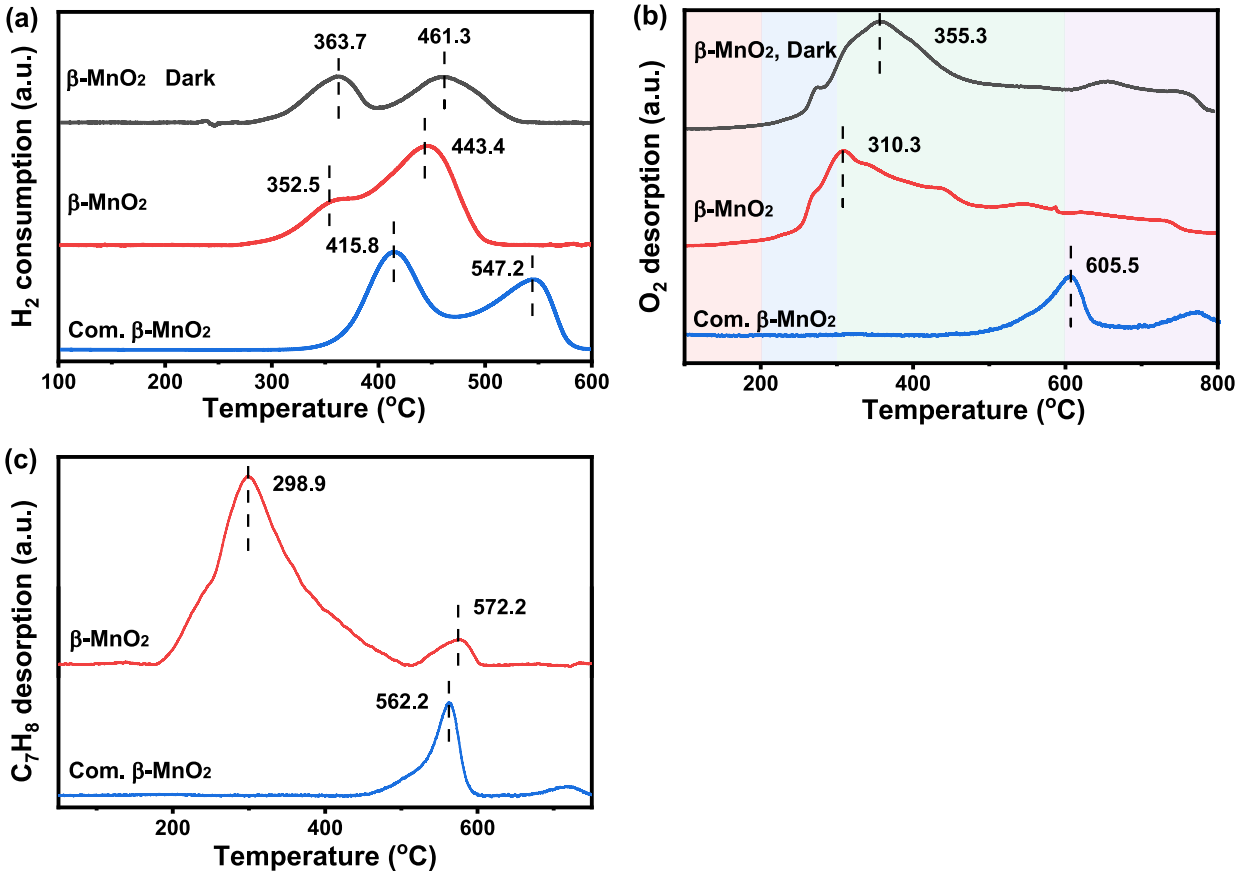


**Fig. 4.** (a) $H_2$-TPR and (b) $O_2$-TPD profiles of the samples under illumination and in the dark; (c) toluene- TPD profiles of the samples in the dark.

surface oxygen species. This shift originates from photogenerated electrons reducing $Mn^{4+}$ to $Mn^{3+}$, weakening Mn—O bonds and lowering oxygen desorption barriers [23]. In contrast, light-irradiated Com.β-$MnO_2$ showed a dominant high-temperature peak at 605.5 °C, reflecting tightly bound subsurface oxygen and limited reactivity. Notably, β-$MnO_2$ exhibited a ~ 295.2 °C lower desorption temperature and larger peak area than Com.β-$MnO_2$, affirming its superior stabilization of reactive oxygen intermediates ($O_{ads.}/O^-$). This aligns with XPS, Raman and EPR data, wherein elevated $O_{vac.}$ content and mixed $Mn^{3+}/Mn^{4+}$ states promote electron transfer to adsorbed $O_2$, facilitating its dissociation into reactive radicals [33]. These properties are pivotal for ambient-temperature VOCs degradation [40].

The influence of defect engineering on pollutant adsorption was further probed by toluene-TPD (Fig. 4c). Synthesized β-$MnO_2$ nanorods exhibited a distinct toluene desorption peak at 298.9 °C, contrasting sharply with Com.β-$MnO_2$, where desorption occurred at 562.2 °C with lower intensity. This 263 °C reduction signifies significantly weakened toluene binding affinity on the defect-engineered surface, attributable to synergistic effects of $O_{vac.}$ and the mesoporous architecture. The higher peak intensity further correlates with the enlarged specific surface area, confirming abundant accessible adsorption sites and favorable mass transfer kinetics.

### 3.4. Photocatalytic degradation performance under visible light

The photocatalytic performance of defect-engineered β-$MnO_2$

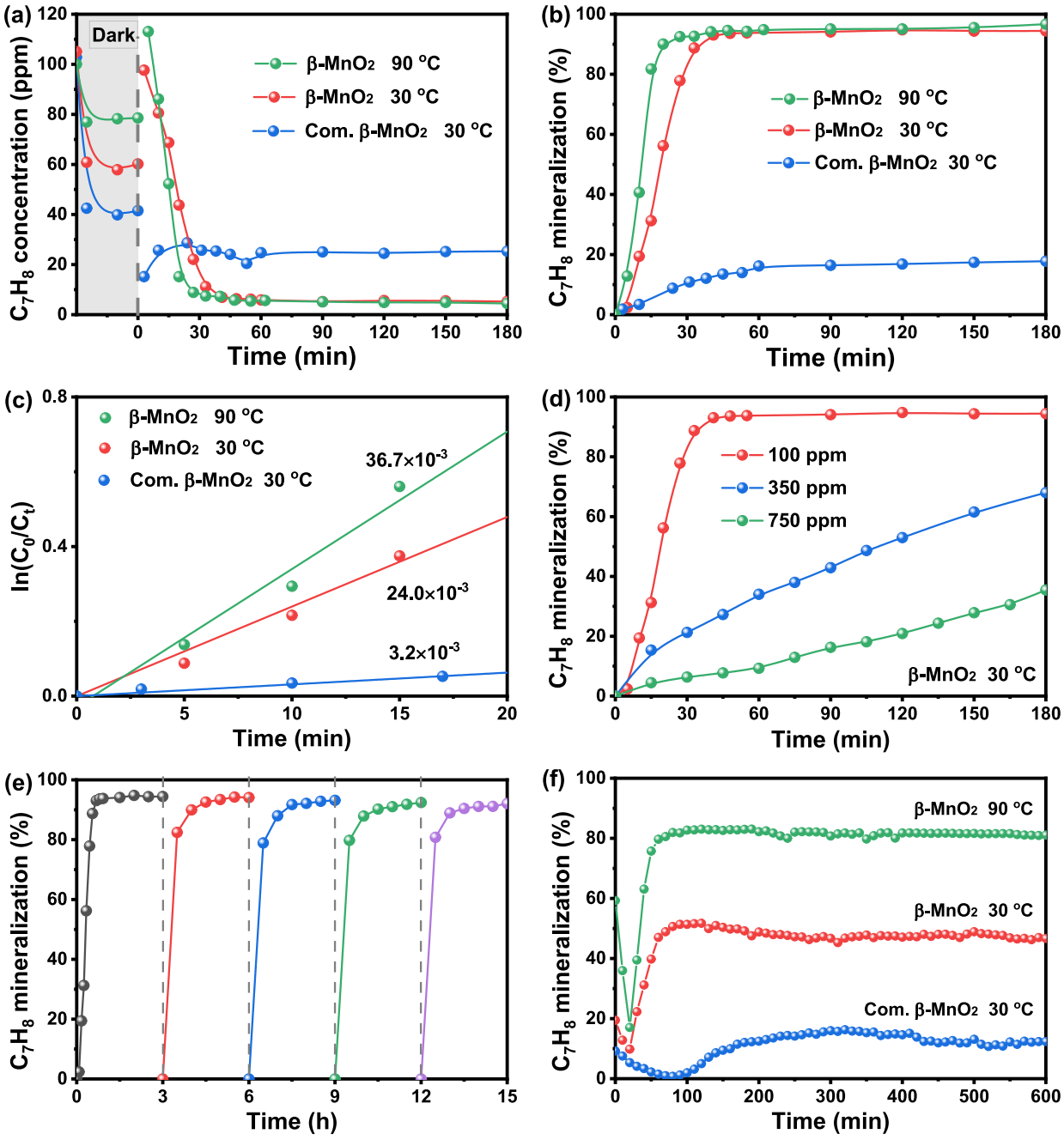


**Fig. 5.** (a, b) Photocatalytic degradation of 100 ppm toluene over the samples in batch reactor at 30 and 90 °C, and (c) their pseudo-first-order kinetics; (d) Photocatalytic mineralization of toluene with different concentrations over β-$MnO_2$ nanorods at 30 °C; (e) Cyclic stability test for photocatalytic mineralization of 100 ppm toluene over β-$MnO_2$ at 30 °C, (f) Time-dependent toluene mineralization over the samples in continuous photocatalytic reactor at 30 and 90 °C.

nanorods was evaluated through the degradation of gaseous toluene under visible light irradiation at ambient temperature. Following a 30-min dark period to establish adsorption-desorption equilibrium, β-$MnO_2$ reduced toluene concentration from 100 ppm to ~60 ppm. In contrast, Com.β-$MnO_2$ showed stronger adsorption, lowering the concentration to ~40 ppm (Fig. 5a), attributed to its confined pore structure favoring physical adsorption (Fig. S1). However, this structure also hindered toluene desorption. Upon illumination, β-$MnO_2$ nanorods facilitated rapid desorption, restoring the concentrations to ~100 ppm, whereas negligible desorption occurred with Com.β-$MnO_2$. Crucially, the defect-engineered β-$MnO_2$ achieved 95 % toluene degradation and 93 % mineralization within 40 min (Fig. 5a,b), exhibiting 7.2 times higher mineralization efficiency than Com.β-$MnO_2$ (~12.9 %). This high selectivity toward complete oxidation to $CO_2$ minimized harmful intermediates.

Elevating the temperature to 90 °C under visible light (photothermal catalysis) significantly accelerated kinetics. While dark adsorption was stronger at 30 °C, irradiation at 90 °C suppressed adsorption but enhanced degradation, achieving >95 % degradation/mineralization within 30 min (Fig. 5b). Kinetic analysis using a pseudo-first-order model (Fig. 5c) revealed apparent rate constants of 24.0 × $10^{-3}$ $min^{-1}$ at 30 °C and 36.7 × $10^{-3}$ $min^{-1}$ at 90 °C, indicating a 1.5-fold photothermal enhancement for 100 ppm toluene.

This photothermal synergy was markedly amplified at higher toluene concentrations. Under ambient temperature (30 °C), mineralization efficiency decreased with increasing initial concentration (100–750 ppm, Fig. 5d). However, at 90 °C, the apparent rate constant surged from 1.8 × $10^{-3}$ $min^{-1}$ at 30 °C to 10.0 × $10^{-3}$ $min^{-1}$ at 90 °C for 750 ppm toluene, representing a 5.6-fold increase (Fig. S3). This contrasts with the mere 1.5-fold enhancement observed for 100 ppm under identical conditions (Fig. 5c), demonstrating that photothermal synergy scales with toluene concentration in low-to-medium temperature regimes. This concentration-dependent mechanism favors high-concentration VOCs remediation. Specifically, elevated temperature (90 °C) weakens toluene adsorption affinity (Fig. 4c), mitigating active-site blockage and promoting rapid desorption of intermediates. Concurrently, accelerated $Mn^{3+}/Mn^{4+}$ redox cycling (Fig. 4a) sustains radical flux ($\bullet O_2^-$/•OH) to meet the heightened oxidative demand for concentrated toluene. Enhanced diffusion through mesoporous channels (Fig. S1) further ensures efficient mass transfer to defect-active sites.

Cycling stability tests (Fig. 5e) confirmed the exceptional durability of β-$MnO_2$ nanorods. Over five successive cycles under visible light, the catalyst retained >90 % mineralization efficiency, demonstrating negligible performance decay. Continuous-flow reactor studies further highlighted its superior stability performance (Fig. 5f). At 30 °C, β-$MnO_2$ nanorods achieved ~50 % mineralization within 60 min under dynamic flow conditions. This lower mineralization efficiency compared to batch mode (93 % at 40 min) stems from reduced residence time in the continuous-flow system, limiting pollutant-catalyst contact and preventing full adsorption-desorption equilibrium. Notably, β-$MnO_2$ nanorods significantly outperformed Com.β-$MnO_2$ (~15 % after 300 min) and benchmark P25 (~23 % after 300 min, Fig. S4) under identical continuous-flow conditions. More than 2 times enhancement over P25 highlights the superiority of defect-engineered β-$MnO_2$ nanorods for gaseous toluene mineralization. Remarkably, elevating the temperature to 90 °C under irradiation substantially accelerated kinetics, enabling ~80 % mineralization within 50 min. Negligible mineralization occurred in the dark at 90 °C (Fig. S5), confirming that thermal energy alone is insufficient but synergistically enhances the photo-initiated, defect-mediated process. Moreover, The catalyst maintained high activity without deactivation over 10 h of continuous operation, validating stability across batch and flow systems. Post-reaction HRTEM, XRD and EPR (Figs. S6–S7) confirmed retention of nanostructure, phase purity, and $O_{vac.}$, underscoring structural robustness.

### 3.5. Reaction mechanism underpinning defect-enhanced photocatalysis

The exceptional photocatalytic mineralization performance of defect-engineered β-$MnO_2$ nanorods arises from the synergistic integration of tailored nanoscale morphology, compressive lattice strain, and strategically introduced defects, which collectively optimize charge dynamics, oxygen activation, and reactant accessibility. This mechanistic framework is substantiated by spectroscopic and kinetic evidence, including in situ monitoring of intermediate species.

#### 3.5.1. Defect-mediated charge separation and radical generation

Preferential [001]-oriented growth (Fig. 1a,b) establishes directional charge-transport highways. This minimizes recombination losses while efficiently delivering photogenerated electrons to active sites [41]. Concurrently, compressive lattice strain, evidenced by the 7 $cm^{-1}$ Raman blue shift (Fig. 2a), shortens Mn—O bonds. This structural modulation enhances hole migration through oriented $Mn^{4+}$–$O^-$ dipoles. Critically, $O_{vac.}$ function as effective electron reservoirs, confirmed by light-induced amplification of the EPR signal at g = 2.003 (Fig. 3b), assigned to paramagnetic $V_O^{\bullet}$ centers. This traps photogenerated electrons, suppressing charge recombination. Furthermore, the elevated $Mn^{3+}$ content (47.2 %, Table S2) introduces mid-gap states that trap photogenerated holes, oxidizing $Mn^{3+}$ to $Mn^{4+}$. Simultaneously, $Mn^{3+}$ species donates electrons to adsorbed $O_2$ at adjacent sites, generating $\bullet O_2^-$ radicals. This dual-path mechanism, involving $O_{vac.}$ electron capture and $Mn^{3+}$ hole trapping, enables sustained electron transfer to $O_2$ adsorbed at $O_{vac.}$ sites, driving efficient $\bullet O_2^-$ formation, as validated by intensified DMPO-$\bullet O_2^-$ EPR signals (Fig. 3f). The cyclic $Mn^{3+}/Mn^{4+}$ interconversion inherent in this process perpetuates both charge separation and radical generation.

#### 3.5.2. Defect-activated oxygen dynamics and adsorption optimization

$O_{vac.}$ and $Mn^{3+}/Mn^{4+}$ cycling fundamentally reconfigure oxygen activation pathways. $H_2$-TPR profiles (Fig. 4a) reveal a 63 °C reduction peak shift relative to Com.β-$MnO_2$, confirming $O_{vac.}$-mediated destabilization of lattice oxygen and accelerated redox cycling. $O_2$-TPD analysis (Fig. 4b) further demonstrates a ~ 295 °C decrease in oxygen desorption energy, promoting abundant reactive oxygen species ($O_{ads.}/O^-$) [40] critical for ambient-temperature catalysis. Complementarily, the nanorod morphology (16-fold higher surface area; 52.62 $m^2 \cdot g^{-1}$) and slit-shaped mesopores facilitate rapid toluene diffusion to defect-rich interfaces [42]. Lattice strain and vacancies cooperatively polarize toluene C—H bonds, weakening adsorption affinity as directly evidenced by toluene-TPD (Fig. 4c): a 263 °C lower desorption peak (298.9 °C for β-$MnO_2$ and 562.2 °C for Com.β-$MnO_2$) prevents active-site blockage and enables efficient oxidation turnover.

#### 3.5.3. Defect-enhanced photocatalytic mineralization performance

During photocatalysis, photogenerated holes oxidize surface $Mn^{3+}$ to $Mn^{4+}$, replenishing active centers while releasing protons for •OH formation. Simultaneously, electrons reduce adsorbed $O_2$ at $O_{vac.}$ sites, generating $\bullet O_2^-$ radicals (Fig. 6a). EPR spin-trapping confirms significantly enhanced $\bullet O_2^-$ and •OH generation over the defect-engineered β-$MnO_2$ nanorods compared to the commercial counterpart (Fig. 3e,f). A quantitative correlation between defect density and activity further validates this defect-mediated mechanism. As summarized in Table S4, the engineered β-$MnO_2$ nanorods exhibit 66.7 % higher $O_{vac.}$ concentration and 19.5 higher $Mn^{3+}$ content relative to Com.β-$MnO_2$, accompanied by a 3.1-fold stronger light-induced EPR signal (g = 2.003). These enhancements directly correlate with a 7.5-fold increase in the apparent rate constant (24.0 × $10^{-3}$ $min^{-1}$ vs. 3.2 × $10^{-3}$ $min^{-1}$). The observed nonproportional activity-defect relationship suggests synergistic effects between $O_{vac.}$ and $Mn^{3+}/Mn^{4+}$ redox couples: $O_{vac.}$ traps electrons to suppress recombination, while $Mn^{3+}$ sites facilitate hole transfer and oxygen activation (Fig. 3e,f). This synergy maximizes the utilization of photogenerated carriers, accounting for the

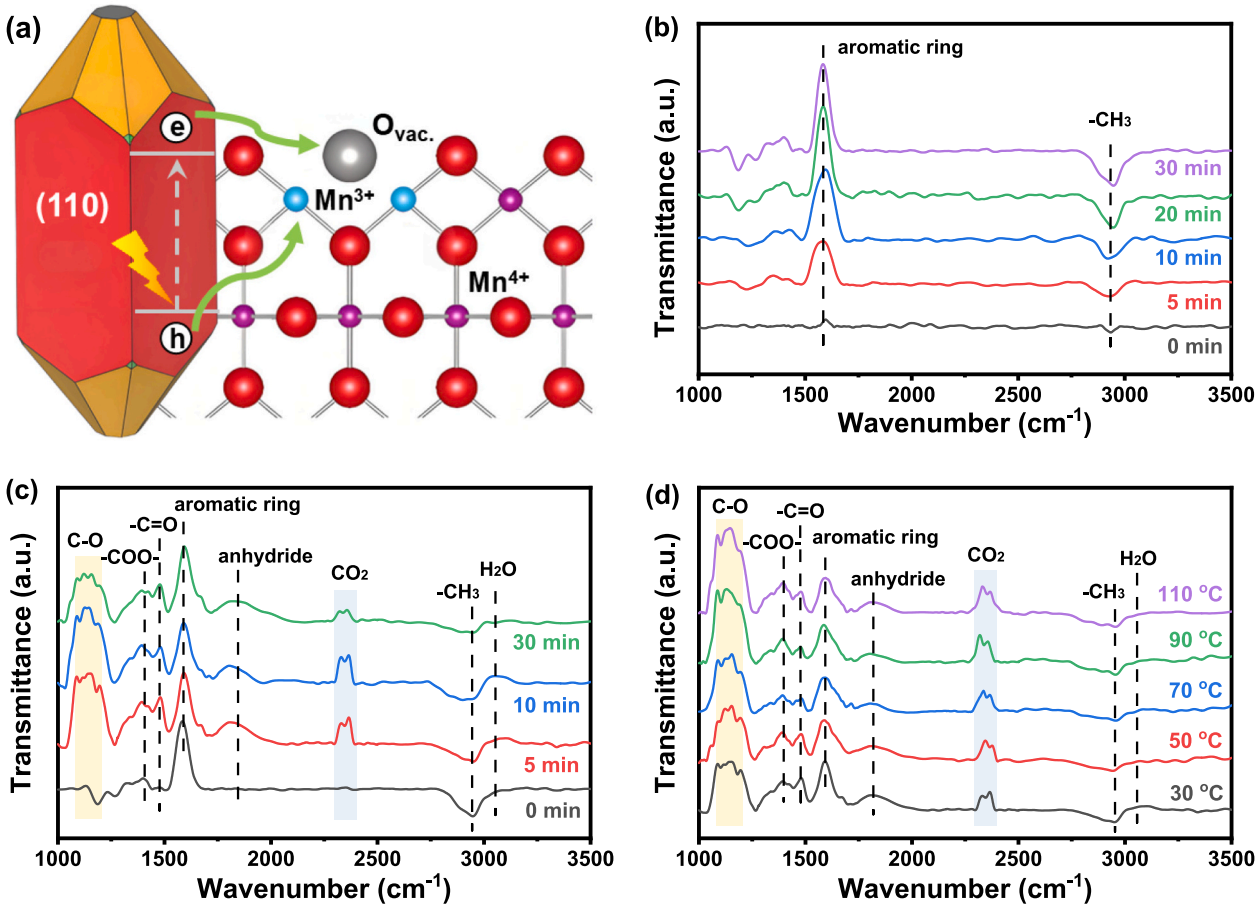


**Fig. 6.** (a) Directional charge separation and transport in defect-engineered β-$MnO_2$ nanorods; in situ DRIFTS curves of (b) toluene adsorption and (c) photocatalytic oxidation of toluene with different time intervals at 30 °C; (d) temperature-dependent photocatalytic oxidation of toluene over β-$MnO_2$ nanorods.

disproportionate activity enhancement relative to defect concentration alone. These confined defect clusters within the nanorods create integrated reaction microenvironments. Within these zones, directional charge transport, optimized oxygen activation, and efficient mass transfer collectively enable near-complete toluene mineralization, achieving 93 % efficiency at ambient temperature within 40 min. Photothermal synergy at 90 °C further accelerates kinetics by thermally promoting charge transfer, $Mn^{3+}/Mn^{4+}$ cycling, and radical mobility. Concurrently, thermal energy facilitates toluene desorption and diffusion to defect-active sites, ensuring continuous catalytic turnover even under high pollutant loads (750 ppm, Fig. 5d). In stark contrast, Com.β-$MnO_2$ exhibits fundamental limitations: agglomerated micropores restrict mass transfer and active site accessibility, while its low defect density (9.6 % $O_{vac.}$) and inert surface impede charge separation, oxygen activation, and catalytic cycling. Consequently, it achieves only minimal mineralization (~13 %) with significant residual toluene (~30 ppm), highlighting the critical role of defect engineering and nanoscale morphology in enabling efficient VOCs remediation.

### 3.5.4. *Defect-driven mineralization pathway*

In situ DRIFTS analysis unequivocally demonstrates the critical role of defects in enabling deep oxidation (Fig. 6b–d). Under dark conditions, initial spectra showed negligible toluene features. However, characteristic bands, including C═C ring vibrations at 1597 $cm^{-1}$ (typical aromatic ring peaks) and -$CH_3$ stretches at 2933 $cm^{-1}$ [43], progressively intensified, confirming rapid surface adsorption. Upon visible-light illumination, key intermediate bands emerged: C—O stretches of primary alcohol (1088/1201 $cm^{-1}$, benzyl alcohol), benzaldehyde (1485 $cm^{-1}$), benzoic acid (1409 $cm^{-1}$), and anhydride (1842 $cm^{-1}$) [43,44]. While these intermediates initially accumulated, aromatic ring vibrations concurrently weakened as $CO_2$ (2324 $cm^{-1}$) and $H_2O$ (3055 $cm^{-1}$) bands intensified, indicating progressive mineralization. Notably, after ~30 min of illumination, intensities of all intermediate and product bands decreased, accompanied by a resurgence of toluene signals. The resurgence reflects dynamic replenishment of gas-phase toluene onto newly vacated active sites as intermediates mineralize, rather than catalyst deactivation. This transient effect is specific to flow-type DRIFTS and aligns with sustained activity in continuous reactors (Fig. 5f). To quantitatively link the spectroscopic pathway to mineralization, exhaust gas from the DRIFTS cell (after 30 min illumination under identical conditions to Fig. 6c) was collected and analyzed by GC. The measured $CO_2$ concentration (~500 ppm) corresponds to a toluene mineralization efficiency of 7.1 %, providing direct experimental confirmation of deep oxidation to $CO_2$. The spectral evolution demonstrates the oxidation pathway: toluene → benzyl alcohol → benzaldehyde → benzoic acid → anhydride → oxygenated fragments (carboxylates, carbonates) → complete mineralization to $CO_2/H_2O$ [45]. Temperature-dependent DRIFTS studies (30–110 °C) under visible light showed the same intermediates and products. Within this temperature range, the band intensities of intermediates and $CO_2$ generally increased with temperature, indicating enhanced reaction rates. However, the $H_2O$ band intensity decreased at higher temperatures, likely due to increased $H_2O$ consumption for •OH formation under intensified photothermal conditions combined with thermally facilitated $H_2O$ desorption [46].

## 4. Conclusion

This study successfully demonstrates a scalable strategy for synthesizing defect-engineered β-$MnO_2$ nanorods via surfactant-assisted hydrothermal synthesis combined with controlled acidification. This approach concurrently introduces abundant $O_{vac.}$ and stabilizes mixed $Mn^{3+}/Mn^{4+}$ valence states. The synergistic interplay between the nanorod morphology, compressive lattice strain, and these engineered defects significantly enhances visible-light absorption, promotes directional charge transport, suppresses charge recombination, and facilitates efficient oxygen activation into reactive radicals. Consequently, the catalyst achieves exceptional visible-light-driven photocatalytic mineralization of gaseous toluene under ambient conditions, attaining 95 % degradation and 93 % mineralization within 40 min, a 7.2-fold mineralization efficiency enhancement over commercial β-$MnO_2$. In situ DRIFTS analysis confirmed a deep oxidation pathway proceeding through sequential oxidation intermediates (benzyl alcohol, benzaldehyde, benzoic acid) to complete mineralization as $CO_2/H_2O$, confirming defect-mediated deep oxidation. Furthermore, photothermal synergy at 90 °C substantially accelerates reaction kinetics, yielding a 5.6-fold rate increase for high-concentration toluene (750 ppm) degradation while maintaining high mineralization selectivity. The catalyst exhibits robust stability, retaining >90 % efficiency over five consecutive cycles and sustaining high activity during continuous-flow operation for over 10 h. This work provides a cost-effective framework for designing transition metal oxide catalysts with tunable defect structures and morphologies for energy-efficient environmental remediation.

## CRediT authorship contribution statement

**Jiejing Kong:** Writing – review & editing, Supervision, Funding acquisition, Conceptualization. **Hongzhao Chen:** Writing – original draft, Visualization, Investigation. **Zhida Li:** Visualization, Validation. **Miaoqiu Tang:** Validation, Conceptualization. **Yi Wang:** Writing – review & editing, Funding acquisition. **Yunlong Guo:** Writing – review & editing, Funding acquisition. **Weiping Zhang:** Writing – review & editing. **Taicheng An:** Writing – review & editing.

## Declaration of competing interest

The authors declare that they have no known competing financial interests or personal relationships that could have appeared to influence the work reported in this paper.

## Acknowledgments

This work was financially supported by Guangdong Basic and Applied Basic Research Foundation (2024A1515030144, 2022A1515011465, and 2019A1515110413), National Natural Science Foundation of China (42007315, 42377099, and 42377221), as well as Guangzhou Science and Technology Project (2024A04J0596 and 2025A04J5265).

## Appendix A. Supplementary data

Supplementary data to this article can be found online at https://doi.org/10.1016/j.cej.2025.167730.

## Data availability

Data will be made available on request.

## References

[1] H. Huang, Y. Xu, Q. Feng, D. Leung, Low temperature catalytic oxidation of volatile organic compounds: a review, Catal. Sci. Technol. 5 (2015) 2649–2669.
[2] A. Yusuf, C. Snape, J. He, H. Xu, C. Liu, M. Zhao, G. Chen, B. Tang, C. Wang, J. Wang, S. Behera, Advances on transition metal oxides catalysts for formaldehyde oxidation: A review, Catal. Rev. 59 (2017) 189–233.
[3] C. Jiang, D. Li, P. Zhang, J. Li, J. Wang, J. Yu, Formaldehyde and volatile organic compound (VOC) emissions from particleboard: Identification of odorous compounds and effects of heat treatment, Build. Environ. 117 (2017) 118–126.
[4] P. Gong, F. He, J. Xie, D. Fang, Catalytic removal of toluene using $MnO_2$-based catalysts: A review, Chemosphere 318 (2023) 137938.
[5] M. Munoz-Batista, O. Fontelles-Carceller, A. Kubacka, M. Fernandez-Garcia, Effect of exfoliation and surface deposition of $MnO_x$ species in g-$C_3N_4$: Toluene photodegradation under UV and visible light, Appl. Catal. B-Environ. 203 (2017) 663–672.
[6] X. Li, L. Wang, X. Lu, Preparation of silver-modified $TiO_2$ via microwave-assisted method and its photocatalytic activity for toluene degradation, J. Hazard. Mater. 177 (2010) 639–647.
[7] Y. Guo, M. Wen, G. Li, T. An, Recent advances in VOC elimination by catalytic oxidation technology onto various nanoparticles catalysts: a critical review, Appl. Catal. Environ. 281 (2021) 119447.
[8] W. Liu, W. Xiang, N. Guan, R. Cui, H. Cheng, X. Chen, Z. Song, X. Zhang, Y. Zhang, Enhanced catalytic performance for toluene purification over $Co_3O_4/MnO_2$ catalyst through the construction of different $Co_3O_4$-$MnO_2$ interface, Sep. Purif. Technol. 278 (2022) 119590.
[9] J. Torres, J. Giraudon, J. Lamonier, Formaldehyde total oxidation over mesoporous MnOx catalysts, Catal. Today 176 (2011) 277–280.
[10] I. Sophiana, A. Topandi, F. Iskandar, H. Devianto, N. Nishiyama, Y. Budhi, Catalytic oxidation of benzene at low temperature over novel combination of metal oxide based catalysts: CuO, MnO2, NiO with Ce0.75Zr0.25O2 as support, Mater. Today Chem. 17 (2020) 100305.
[11] R. Yang, Y. Fan, R. Ye, Y. Tang, X. Cao, Z. Yin, Z. Zeng, MnO2-based materials for environmental applications, Adv. Mater. 33 (2021) 2004862.
[12] L. Yan, Y. Liu, K. Zha, H. Li, L. Shi, D. Zhang, Scale–activity relationship of $MnO_x$-$FeO_y$ nanocage catalysts derived from prussian blue analogues for low-temperature NO reduction: Experimental and DFT studies, ACS Appl. Mater. Interfaces 9 (2017) 2581–2593.
[13] Y. Zhang, M. Wu, Y. Wang, Y. Kwok, W. Pan, W. Szeto, H. Huang, D. Leung, Fluorinated $TiO_2$ coupling with α-$MnO_2$ nanowires supported on different substrates for photocatalytic VOCs abatement under vacuum ultraviolet irradiation, Appl. Catal. Environ. 280 (2021).
[14] F. Jiang, S. Wang, B. Liu, J. Liu, L. Wang, Y. Xiao, Y. Xu, X. Liu, Insights into the influence of $CeO_2$ crystal facet on $CO_2$ hydrogenation to methanol over Pd/$CeO_2$ catalysts, ACS Catal. 10 (2020) 11493–11509.
[15] K. Vidya Lekshmi, S. Yesodharan, E. Yesodharan, MnO2 efficiently removes indigo carmine dyes from polluted water, Heliyon 4 (2018) e00897.
[16] Z. Rao, G. Lu, L. Chen, A. Mahmood, G. Shi, Z. Tang, X. Xie, J. Sun, Photocatalytic oxidation mechanism of Gas-Phase VOCs: Unveiling the role of holes, •OH and $\bullet O_2^-$, Chem. Eng. J. 430 (2022) 132766.
[17] S. Rong, P. Zhang, J. Wang, F. Liu, Y. Yang, G. Yang, S. Liu, Ultrathin manganese dioxide nanosheets for formaldehyde removal and regeneration performance, Chem. Eng. J. 306 (2016) 1172–1179.
[18] Y. Guo, D. Ye, K. Chen, J. He, W. Chen, Toluene decomposition using a wire-plate dielectric barrier discharge reactor with manganese oxide catalyst in situ, J. Mol. Catal. A-Chem. 245 (2006) 93–100.
[19] L. Miao, J. Wang, P. Zhang, Review on manganese dioxide for catalytic oxidation of airborne formaldehyde, Appl. Surf. Sci. 466 (2019) 441–453.
[20] S. Liang, L. Zheng, L. Song, X. Wang, W. Tu, J. Xu, Accelerated confined mass transfer of MoS2 1D nanotube in photo-assisted metal–air batteries, Adv. Mater. 36 (2024) 202307790.
[21] D. Tompsett, S. Parker, M. Islam, Rutile (β-)MnO2 surfaces and vacancy formation for high electrochemical and catalytic performance, J. Am. Chem. Soc. 136 (2014) 1418–1426.
[22] M. Thommes, K. Kaneko, A. Neimark, J. Olivier, F. Rodriguez-Reinoso, J. Rouquerol, K. Sing, Physisorption of gases, with special reference to the evaluation of surface area and pore size distribution (IUPAC Technical Report), Pure Appl. Chem. 87 (2015) 1051–1069.
[23] E. Vermeersch, F. Kosek, J. De Grave, J. Jehlicka, A. Rousaki, Layered manganese oxides structures: micro-raman and selected mobile raman spectroscopic studies, J. Raman Spectrosc. 55 (2024) 246–262.
[24] C. Julien, M. Massot, R. Baddour-Hadjean, S. Franger, S. Bach, J. Pereira-Ramos, Raman spectra of birnessite manganese dioxides, Solid State Ionics 159 (2003) 345–356.
[25] G. Zhou, W. Geng, L. Sun, X. Wang, W. Xiao, J. Wang, L. Wang, Influence of mixed valence on the formation of oxygen vacancy in cerium oxides, Materials 12 (2019) 4041.
[26] Y. Li, Z. Fan, J. Shi, Z. Liu, W. Shangguan, Post plasma-catalysis for VOCs degradation over different phase structure $MnO_2$ catalysts, Chem. Eng. J. 241 (2014) 251–258.
[27] Y. Zhang, M. Chen, Z. Zhang, Z. Jiang, W. Shangguan, H. Einaga, Simultaneously catalytic decomposition of formaldehyde and ozone over manganese cerium oxides at room temperature: Promotional effect of relative humidity on the $MnCeO_x$ solid solution, Catal. Today 327 (2019) 323–333.
[28] Z. Mo, H. Xu, Z. Chen, X. She, Y. Song, J. Lian, X. Zhu, P. Yan, Y. Lei, S. Yuan, H. Li, Construction of $MnO_2$/Monolayer g-$C_3N_4$ with Mn vacancies for Z-scheme overall water splitting, Appl. Catal. B-Environ. 241 (2019) 452–460.
[29] D. Gangwar, C. Rath, Structural, optical and magnetic properties of α-and β-$MnO_2$ nanorods, Appl. Surf. Sci. 557 (2021) 149693.

[30] K. Ahmed, H. Peng, K. Wu, K. Huang, Hydrothermal preparation of nanostructured manganese oxides (MnOx) and their electrochemical and photocatalytic properties, Chem. Eng. J. 172 (2011) 531–539.
[31] Z. Qu, Y. Bu, Y. Qin, Y. Wang, Q. Fu, The improved reactivity of manganese catalysts by Ag in catalytic oxidation of toluene, Appl. Catal. B Environ. 132 (2013) 353–362.
[32] L. Su, X. Chen, H. Wang, Y. Wang, Z. Lu, Oxygen vacancies promoted heterogeneous catalytic ozonation of atrazine by defective 4A zeolite, J. Clean. Prod. 336 (2022) 130376.
[33] V. Santos, M. Pereira, J. Órfão, J. Figueiredo, The role of lattice oxygen on the activity of manganese oxides towards the oxidation of volatile organic compounds, Appl. Catal. Environ. 99 (2010) 353–363.
[34] B. Solsona, T. Garcia, S. Agouram, G. Hutchings, S. Taylor, The effect of gold addition on the catalytic performance of copper manganese oxide catalysts for the total oxidation of propane, Appl. Catal. B-Environ. 101 (2011) 388–396.
[35] L. Qu, C. Li, G. Zeng, M. Zhang, M. Fu, J. Ma, F. Zhan, D. Luo, Support modification for improving the performance of $MnO_x$–$CeO_y$/γ-$Al_2O_3$ in selective catalytic reduction of NO by $NH_3$, Chem. Eng. J. 242 (2014) 76–85.
[36] Y. Zheng, W. Wang, D. Jiang, L. Zhang, Amorphous $MnO_x$ modified $Co_3O_4$ for formaldehyde oxidation: Improved low-temperature catalytic and photothermocatalytic activity, Chem. Eng. J. 284 (2016) 21–27.
[37] Z. Li, C. Su, Y. Yan, M. Fu, Synthesis of xCe–$MnO_2$ with three-dimensional ultra-thin nanosheet structure and its excellent low-temperature reducibility for toluene catalysis, Environ. Sci. Pollut. Res. 30 (2023) 92238–92254.
[38] A. Bielański, J. Haber, Oxygen in catalysis on transition metal oxides, Catal. Rev. Sci. Eng. 19 (1979) 1–41.
[39] W. Si, Y. Wang, S. Zhao, F. Hu, J. Li, A facile method for in situ preparation of the $MnO_2$/$LaMnO_3$ catalyst for the removal of toluene, Environ. Sci. Technol. 50 (2016) 4572–4578.
[40] Y. Zhang, J. Shi, W. Fang, M. Chen, Z. Zhang, Z. Jiang, W. Shangguan, H. Einaga, Simultaneous catalytic elimination of formaldehyde and ozone over one-dimensional rod-like manganese dioxide at ambient temperature, J. Chem. Technol. Biotechnol. 94 (2019) 2305–2317.
[41] T. Barudžija, V. Kusigerski, N. Cvjetićanin, S. Šorgić, M. Perović, M. Mitrić, Structural and magnetic properties of hydrothermally synthesized β-$MnO_2$ and α-$K_xMnO_2$ nanorods, J. Alloys Compd. 665 (2016) 261–270.
[42] K. Huang, M. Lei, R. Zhang, H. Yang, Y. Yang, Low-temperature route to dispersed manganese dioxide nanorods, Mater. Lett. 78 (2012) 202–204.
[43] Y. Li, T. Chen, S. Zhao, P. Wu, Y. Chong, A. Li, Y. Zhao, G. Chen, X. Jin, Y. Qiu, D. Ye, Engineering cobalt oxide with coexisting cobalt defects and oxygen vacancies for enhanced catalytic oxidation of toluene, ACS Catal. 12 (2022) 4906–4917.
[44] Y. Chong, T. Chen, Y. Li, J. Lin, W. Huang, C. Chen, X. Jin, M. Fu, Y. Zhao, G. Chen, J. Wei, Y. Qiu, G. Waterhouse, D. Ye, Z. Lin, L. Guo, Quenching-induced defect-rich platinum/metal oxide catalysts promote catalytic oxidation, Environ. Sci. Technol. 57 (2023) 5831–5840.
[45] W. Yang, Y. Wang, W. Yang, H. Liu, Z. Li, Y. Peng, J. Li, Surface in situ doping modification over Mn2O3 for toluene and propene catalytic oxidation: the effect of isolated $Cu^{\delta+}$ insertion into the mezzanine of surface $MnO_2$ cladding, ACS Appl. Mater. Interfaces 13 (2021) 2753–2764.
[46] J. Kong, C. Jiang, Z. Rui, S. Liu, F. Xian, W. Ji, H. Ji, Photothermocatalytic synergistic oxidation: An effective way to overcome the negative water effect on supported noble metal catalysts for VOCs oxidation, Chem. Eng. J. 397 (2020) 125485.